Supporting Information for "Perturbation of Electron Velocity Distribution due to Interaction with Chorus Emissions"

DOI: 10.1002/TODO

Miroslav Hanzelka[1,2], Ondřej Santolík[1,2], Yoshiharu Omura[3]

[1]Department of Space Physics, Institute of Atmospheric Physics, Czech Academy of Sciences, Prague, Czech Republic

[2]Faculty of Mathematics and Physics, Charles University, Prague, Czech Republic

[3]Research Institute for Sustainable Humanosphere, Kyoto University, Uji, Japan

Contents of this file

1. Text S1
2. Figures S1 to S2

Additional Supporting Information (Files uploaded separately)

1. Captions for Movies S1 to S5

Introduction

Corresponding author: M. Hanzelka, Department of Space Physics, Institute of Atmospheric Physics, Czech Acad. Sci., Bocni II 1401, 141 00 Praha 4 Sporilov, Czech Republic. (mha@ufa.cas.cz)

Text S1 describes the full equations and input parameters which were used to calculate the chorus wave field for all the test particle simulations conducted in the study. Figure S1 shows an example trajectory of a particle that interacts once with the element propagating left of the equator and then again with the element propagating right of the equator. Figure S2 shows changes in energy and pitch angle, in time and space, of this example particle. Movies S1 to S3 are slideshows showing the time evolution of the electron hole inside the first two subpackets at the equator. They show the phase space density (S1), changes in energy (S2) and changes in pitch-angle (S3). Note that these animations were done for a highly anisotropic Maxwellian-like distribution, so the results could look very different with lower anisotropies or different types of distribution. Movie S4 is a slide show showing the evolution of the velocity distribution $f(v_{\parallel}, v_{\perp})$ at the equator, where each slide is captured at time point between two adjacent subpacket. The purpose of the movie is to show the subsequent overlapping of the stripes of increased and decreased density and the distortion of these stripes due to adiabatic motion. Finally, Movie S5 shows the evolution of relativistic pitch-angle anisotropy. The symbols used in the Supporting Information are explained in the Notation section.

Text S1. To calculate the chorus wave field, which is at the background of all particle simulations conducted in this study, we use the model of Hanzelka, Santolík, Omura, Kolmašová, and Kletzing (2020). In the model it is assumed that the source of each subpacket is a point in space, specifically $h_1 = 0$ for the first subpacket. The amplitude at $t = 0$ is double the threshold amplitude

$$\Omega_{\mathrm{thr}}(h_i) = \frac{5\xi\gamma_{\mathrm{R}}s_2^2}{\chi^5 Q^2 J_{\mathrm{E,max}} S_{\mathrm{max}}} \frac{a^2c^4}{\omega\Omega_{\mathrm{e0}}^2} \left(\frac{\Omega_{\mathrm{e0}}}{\omega_{\mathrm{phe}}}\right)^4 \left(\frac{c}{V_{\perp 0}}\right)^7 \left(\frac{N_{\mathrm{he}}}{c^2 G(h_i)}\right)^2 . \tag{1}$$

The time evolution of frequency and amplitude in the source is described by the coupled equations

$$\left.\frac{\partial\omega}{\partial t}\right|_{h_i} = \frac{S_{\mathrm{max}}s_0\omega}{s_1}\Omega_{\mathrm{w}} - \frac{2ach_i s_2}{s_1}\Omega_{\mathrm{e0}} \tag{2}$$

and

$$\left.\frac{\partial\Omega_{\mathrm{w}}}{\partial t}\right|_{h_i} = \Gamma_{\mathrm{N}}\Omega_{\mathrm{w}} - \frac{2acV_{\mathrm{g}}s_2}{S_{\mathrm{max}}s_0}\frac{\Omega_{\mathrm{e0}}}{\omega} , \tag{3}$$

where

$$\Gamma_{\mathrm{N}} = \frac{(2\xi\chi^3)^{\frac{1}{2}} Q J_{\mathrm{E,max}}}{\gamma_{\mathrm{R}}^{\frac{1}{2}}} \frac{\Omega_{\mathrm{e0}}^2}{(\Omega_{\mathrm{w}}\omega)^{\frac{1}{2}}} \left(\frac{\omega_{\mathrm{phe}}}{\Omega_{\mathrm{e0}}}\right)^2 \frac{V_{\mathrm{g}}}{c} \left(\frac{V_{\perp 0}}{c}\right)^{\frac{5}{2}} \frac{c^2 G}{N_{\mathrm{he}}} \tag{4}$$

is the nonlinear growth rate. When the optimum amplitude

$$\Omega_{\mathrm{opt}}(h_i) = \frac{J_{\mathrm{B,max}}\chi^2 Q s_1}{2^{\frac{1}{2}}\pi S_{\mathrm{max}}\gamma_{\mathrm{R}}\tau s_0} \frac{\Omega_{\mathrm{e0}}^2}{\omega} \left(\frac{\omega_{\mathrm{phe}}}{\Omega_{\mathrm{e0}}}\right)^2 \frac{V_{\mathrm{g}}}{c} \left(\frac{V_{\perp 0}}{c}\right)^3 \frac{c^2 G(h_i)}{N_{\mathrm{he}}} + \frac{2ach_i s_2}{S_{\mathrm{max}}s_0}\frac{\Omega_{\mathrm{e0}}}{\omega} . \tag{5}$$

is reached, the sign of the amplitude growth is switched in order to simulate saturation and decrease in amplitude. A new subpacket is assumed to be triggered by residual resonant current at a point (t_2, h_2) from which the wave would propagate (according to cold plasma dispersion) to the exact point where the amplitude of the previous subpacket drops below Ω_{thr}. The propagation of wave amplitude and frequency in space and time is described

by advection equations

$$\frac{\partial \omega}{\partial t} + V_{\mathrm{g}} \frac{\partial \omega}{\partial h} = 0\,, \tag{6}$$

$$\frac{\partial B_{\mathrm{w}}}{\partial t} + V_{\mathrm{g}} \frac{\partial B_{\mathrm{w}}}{\partial h} = -\frac{\mu_0 V_{\mathrm{g}}}{2} J_E\,. \tag{7}$$

The resonant current component parallel with the wave electric field is given by

$$J_E = -J_0 \int_{\zeta_1}^{\zeta_2} (\cos\zeta_1 - \cos\zeta + S(\zeta - \zeta_1))^{\frac{1}{2}} \sin\zeta \mathrm{d}\zeta\,, \tag{8}$$

where

$$J_0 = \left(\frac{2^3 e^2 V_{\perp 0}^5 \Omega_{\mathrm{w}}}{k \gamma_{\mathrm{R}}} \right)^{\frac{1}{2}} \chi Q G \tag{9}$$

and ζ_1, ζ_2 are given by the shape of the electron phase space hole (Omura et al., 2008). The hot electron distribution function enters the calculation through the quantity

$$G(h) = \left(\frac{1 + ah^2}{1 + ah^2(1 + A_{\mathrm{eq}})} \right)^{\frac{1}{2}} \frac{N_{\mathrm{he}}}{2\pi^2 U_{\perp \mathrm{eq}} U_{\parallel \mathrm{eq}}} \exp\left(-\frac{\gamma_{\mathrm{R}}^2 V_{\mathrm{R}}^2}{2 U_{\parallel \mathrm{eq}}^2} \right)\,. \tag{10}$$

We obtained $G(h)$ through methods described in Summers, Omura, Miyashita, and Lee (2012) using a parabolic approximation of the Earth's dipole magnetic field model and the distribution function

$$f(u_\parallel, u_\perp, h) = \frac{N_{\mathrm{he}}(h)}{(2\pi)^{\frac{2}{3}} U_\parallel U_\perp^2} \exp\left(-\frac{u_\parallel^2}{2U_\parallel^2} - \frac{u_\perp^2}{2U_\perp^2} \right) \tag{11}$$

with hot electron density

$$N_{\mathrm{he}}(h) = \frac{N_{\mathrm{he}}(0) U_\perp^2(h)}{U_{\perp \mathrm{eq}}^2} \tag{12}$$

and perpendicular thermal velocity

$$U_\perp(h) = \left(\left(1 - \frac{B_{\mathrm{eq}}}{B(h)} \right) \frac{1}{U_\parallel^2} + \frac{B_{\mathrm{eq}}}{B(h)} \frac{1}{U_{\perp \mathrm{eq}}} \right)^{-\frac{1}{2}}\,. \tag{13}$$

This is the same distribution as used in the particle simulations.

In the work of Hanzelka et al. (2020) each new subpacket was let to evolve independently of the previous subpacket. But the electron hole structure which produces the resonant current has a certain width in the velocity space, and so if two waves that experience non-linear growth are overlapping, they need to comply to the frequency separability criterion (Omura, Nakamura, Kletzing, Summers, and Hikishima (2015), Equations 36 through 39). In our model, each new subpacket is triggered at such point in time and space that during its propagation, it does not collide with the source of the previous packet in the time-space diagram. However, the model includes a certain overlap of frequency ranges of each two adjacent subpacket. Therefore, during the downstream propagation, adjacent packets will inevitably start merging due to difference in group velocities. We assume that in the overlapping region, the production of resonant current in the new subpacket is supressed, thus limiting the convective growth prescribed by Equation 7. In practice we multiply the resonant current calculated at point (t, h) of the $(i+1)$-th subpacket, overlapping with the i-th subpacket, by a factor

$$\begin{aligned} s_J^{i+1}(t,h) &= \cos^2\left(\frac{\pi}{2}\delta\omega(t,h)\right) \quad \text{for} \quad \delta\omega \in [0,1]\,, \\ &= 0 \quad \text{for} \quad \delta\omega > 1\,, \\ &= 1 \quad \text{for} \quad \delta\omega < 0\,, \end{aligned} \tag{14}$$

where

$$\delta\omega = \frac{\Delta\omega - (\omega^{i+1} - \omega^i)}{\Delta\omega}\,, \tag{15}$$

$\Delta\omega$ is the estimated frequency bandwidth corresponding to the trapping potential as derived by Omura et al. (2015) and ω^i is the frequency of the i-th subpacket. This means

that the resonant current in the $(i+1)$-th subpacket is progressively more suppressed when the frequency separation $(\omega^{i+1} - \omega^i)$ drops below the limiting bandwidth of $\Delta\omega$. In Figure 1a we can see that with this suppression of current, the wave amplitudes B_w reach about $3 \cdot 10^{-3} B_\mathrm{eq}$ at the equator and increase by less than a factor of 2 after reaching magnetic latitude $\lambda_\mathrm{m} = 10°$. The first subpacket is an outlier as the simulation proceeds sequentially, subpacket by subpacket, and thus we cannot apply the factor s_J to the first wave. However, the convective growth results in a maximum amplitude of about $1.3 \cdot 10^{-2} B_\mathrm{eq}$ (Figure 1b), which is comparable to the most intense whistler waves observed in the inner magnetosphere (Kellogg et al., 2011). Also, wave amplitudes inside chorus elements tend to be the highest in the first few subpackets – see Figure 4b in Santolík, Kletzing, Kurth, Hospodarsky, and Bounds (2014).

Finally, the evolution equations are solved by the upwind method with time step $\Delta t = 4\,\Omega_\mathrm{e0}^{-1}$ and spatial step $\Delta h = 1\,c\Omega_\mathrm{e0}^{-1}$. The equatorial strength of the dipole field at the surface of the Earth is chosen as $B_\mathrm{sfc} = 3.1 \cdot 10^{-5}\,\mathrm{T}$, L-value of the field line is $L = 4.5$. Further parameters are chosen as follows: $S_\mathrm{max} = 0.41$, $Q = 0.5$, $\tau = 0.25$, $\omega_\mathrm{pe} = 7.0\,\Omega_\mathrm{e0}$, $\omega_\mathrm{phe} = 0.3\,\Omega_\mathrm{e0}$, $V_{\perp 0} = 0.3\,c$, $U_\parallel = 0.12\,c$.

Movie S1. Evolution of the electromagnetic phase space hole at the equator inside the first two subpackets, for particles with perpendicular velocity $v_\perp = 0.25\,c$. The coordinate zeta is the angle between the wave magnetic field vector and the perpendicular particle velocity. We can see the particles from low density region (higher values of $|v_\parallel|$) being trapped and transported to a higher density region, while the particles from high density region (lower values of $|v_\parallel|$) stream along the hole into a lower density region. At the

end of the first subpacket, we can see that two regions of increased and decreased density have been created. The same structure would appear for each perpendicular velocity, but slightly shifted due to dependence of resonance velocity on $v_\perp$ (resonance velocity for $v_\perp = 0.25\,c$ is plotted as a dashed black line in the animation). As a result, the remnant of the phase space hole creates a stripe in velocity distribution as shown in Figure 2. The animation of the evolution of the electromagnetic hole in the second subpacket follows (with a change in vertical axis range and ranges of $f - f_0$), showing the mixing of the high and low density populations created by the first subpacket. The sampling of each frame of the animation is 512 points in $v_\parallel$ and 512 points in φ for each subpacket.

Movie S2. Changes in particle kinetic energy E_k around the electromagnetic phase space hole, same input data as in Movie S1. Kinetic energy of trapped particles is increased. The maximum change increase in energy with respect to the energy before interaction $E_{\mathrm{k}0}$ is about $2.5 \cdot 10^{-3}\,mc^2 = 1.3\,\mathrm{keV}$ for the first subpacket and $4.4 \cdot 10^{-3}\,mc^2 = 2.2\,\mathrm{keV}$ for the second. Energy of untrapped resonant particles has decreased.

Movie S3. Changes in particle equatorial pitch angle α_eq around the electromagnetic phase space hole, same input data as in Movie S1. Pitch angle of trapped particles is increased. The maximum change increase in energy with respect to the equatorial pitch angle before interaction $\alpha_{\mathrm{eq}0}$ is about 12° for the first subpacket and 22.5° for the second. Pitch angle of untrapped resonant particles has decreased.

Movie S4. Evolution of the 2D velocity distribution $f(v_\parallel, v_\perp)$, frames captured after each subpacket at $h = 0$. Each new stripe is getting less and less clear, as the resonance widths

of the adjacent subpackets overlap and cause phase mixing. The decrease in density at the rightmost part of the perturbed region stays clearly visible during the whole evolution.

Movie S5. Evolution of relativistic pitch-angle anisotropy, same time and position as in Movie S4. Due to lack of interparticle interactions, we can assume that the maxima and minima of anisotropy are exaggerated, as the sharp gradients on the edges of the stripes in $f(v_\parallel, v_\perp)$ do not get smoothed out in time. The dashed grey line shows $\omega_{\rm res}$, the frequency of a whistler wave that would resonate with electrons at given parallel velocity and zero perpendicular velocity. The decrease in anisotropy at low $|v_\parallel|$ roughly corresponds to the frequency range of the last subpacket.

Notation

a	factor appearing in the parabolic approximation of the background magnetic field $B = B_{\rm eq}(1 + ah^2)$.
$A_{\rm eq}$	equatorial temperature anisotropy.
$B_{\rm w}$	amplitude of wave magnetic field.
c	speed of light in vacuum.
e	elementary charge.
h_i	position of the source of the i-th subpacket along the field line.
J_E	resonant current component parallel with the wave electric field.
J_B	resonant current component parallel with the wave magnetic field.
$J_{\rm E,max}$	$-J_E$ computed for $S = -S_{\rm max}$.

$J_{\mathrm{B,max}}$ $-J_B$ computed for $S = -S_{\mathrm{max}}$.

k wave number.

m electron mass.

N_{he} hot electron number density.

Q depth of the electron phase space hole.

s_0, s_1, s_2 factors entering the calculation of the inhomogeneity S.

S inhomogeneity ratio from Omura et al. (2008).

S_{eq} negative value of the inhomogeneity ratio in the source.

$u_{\parallel}$ parallel relativistic particle velocity.

$u_{\perp}$ perpendicular relativistic particle velocity.

$U_{\parallel}$, $U_{\parallel\mathrm{eq}}$ parallel thermal relativistic velocity, with subscript 'eq' denoting the equatorial value.

$U_{\perp}$, $U_{\perp\mathrm{eq}}$ perpendicular thermal relativistic velocity, with subscript 'eq' denoting the equatorial value.

V_{g} group velocity of whistler mode wave.

V_{R} cyclotron resonance velocity.

$V_{\perp 0}$ typical perpendicular velocity of particles, appears in the nonlinear growth theory in the function $\delta(V_{\perp 0})$ which replaces the perpendicular factor of the electron velocity distribution function.

γ Lorentz factor.

γ_{R} Lorentz factor for $v_{\parallel=V_{\mathrm{R}}}$.

Γ_{N} nonlinear growth rate.

ζ difference between wave magnetic field phase and perpendicular particle velocity phase.

μ_0 vacuum permeability.

ω wave angular frequency.

Ω_{w} normalized wave amplitude $B_{\mathrm{w}}e/m$.

References

Hanzelka, M., Santolík, O., Omura, Y., Kolmašová, I., & Kletzing, C. A. (2020). A model of the subpacket structure of rising tone chorus emissions. doi: 10.1002/essoar.10503189.1

Kellogg, P. J., Cattell, C. A., Goetz, K., Monson, S. J., & Wilson, I., L. B. (2011, September). Large amplitude whistlers in the magnetosphere observed with Wind-Waves. *Journal of Geophysical Research (Space Physics)*, *116*(A9), A09224. doi: 10.1029/2010JA015919

Omura, Y., Katoh, Y., & Summers, D. (2008, April). Theory and simulation of the generation of whistler-mode chorus. *Journal of Geophysical Research (Space Physics)*, *113*, A04223. doi: 10.1029/2007JA012622

Omura, Y., Nakamura, S., Kletzing, C. A., Summers, D., & Hikishima, M. (2015, September). Nonlinear wave growth theory of coherent hiss emissions in the plasmasphere. *Journal of Geophysical Research (Space Physics)*, *120*(9), 7642-7657. doi: 10.1002/2015JA021520

Santolík, O., Kletzing, C. A., Kurth, W. S., Hospodarsky, G. B., & Bounds, S. R. (2014, January). Fine structure of large-amplitude chorus wave packets. *Geophysical Research Letters*, *41*, 293-299. doi: 10.1002/2013GL058889

Summers, D., Omura, Y., Miyashita, Y., & Lee, D.-H. (2012, Sep). Nonlinear spatiotemporal evolution of whistler mode chorus waves in Earth's inner magnetosphere. *Journal of Geophysical Research (Space Physics)*, *117*(A9), A09206. doi: 10.1029/2012JA017842

Figure S1. Trajectory of a particle that experiences resonant interaction with both chorus elements, superimposed on the wave field. The orange section of the curve, A, denotes the region of interaction with the left-propagating wave. Due to successive trapping in each subpacket (nonlocal process), the parallel velocity $|v_{\parallel}|$ of the particle decreases. In region B (green color) the particle interacts with higher frequency subpackets of the right-propagating wave. In the case depicted here the interaction results in scattering of the particle (local process). Sidenote: the wave field is showing clear standing wave patterns in the region where the two elements overlap. They do not affect cyclotron resonant interaction.

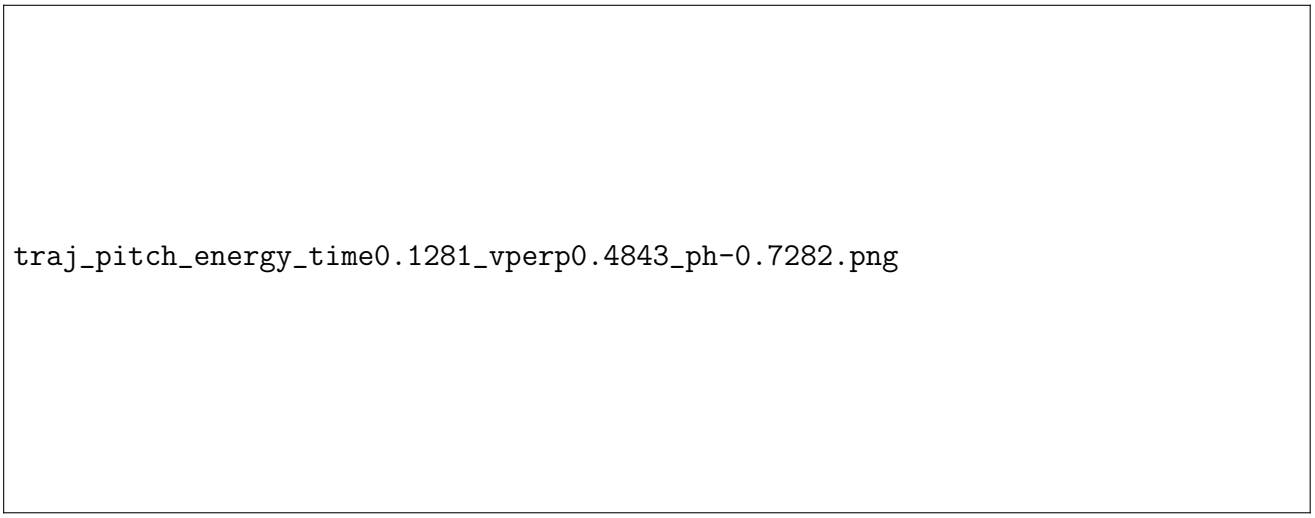

Figure S2. Changes in kinetic energy (a) and equatorial pitch angle (b) along particle trajectory from Figure S1. The nature of the interactions in regions A and B is now very apparent, showing increase in energy and pitch angle in the first interaction (successive trapping) and decrease of energy and pitch angle in the second interaction (resonant scattering).